
SIMULATION OF SCANNING NEAR-FIELD OPTICAL MICROSCOPY SPECTRA OF 1D PLASMONIC GRAPHENE JUNCTIONS

Vyacheslav Semenenko

Department of Electrical Engineering,
University at Buffalo, Buffalo, NY 14260, USA

Mengkun Liu

Department of Physics and Astronomy,
Stony Brook University,
Stony Brook, NY 11794, USA

Vasili Perebeinos

Department of Electrical Engineering,
University at Buffalo, Buffalo, NY 14260, USA
vasilipe@buffalo.edu

August 26, 2021

ABSTRACT

We present numerical simulations of scattering-type Scanning Near-Field Optical Microscopy (s-SNOM) of 1D plasmonic graphene junctions. A comprehensive analysis of simulated s-SNOM spectra is performed for three types of junctions. We find conditions when the conventional interpretation of the plasmon reflection coefficients from s-SNOM measurements does not apply. Our results are applicable to other conducting 2D materials and provide a comprehensive understanding of the s-SNOM techniques for probing local transport properties of 2D materials.

1 Introduction

Scattering type Scanning Near-Field Microscopy (s-SNOM) is a powerful tool for studying local electronic properties of surfaces and 2D materials in a few-nanometer-size domain [1, 2, 3]. Simulation of the s-SNOM signal obtained in experiments is an essential part of a technique for retrieving materials' physical properties. The available mathematical modelings of s-SNOM experiments are developed mainly for homogeneous surfaces [4, 5, 6, 7, 8, 9]. Similar calculations for the case of a composite wafer of planar layers covered by graphene and exciting both by spherical [10, 11] and cylindrical [12] tips have also been reported. Besides, one can find reports of simulated s-SNOM of 1D graphene plasmon junctions [13, 14].

Currently, the most common application of s-SNOM is a visualization of electric properties of surfaces and atomically thin 2D materials. The s-SNOM images give a good qualitative understanding of a sensed object. However, retrieving accurate quantitative information on the length scale beyond the plasmon wavelengths is still a challenge. Some progress in this direction is offered by machine learning techniques [15]. The plasmon's reflectance is one of the most valuable physical quantities of interest [13, 1]. In graphene, plasmon reflectance was reported both analytically and numerically for various types of 1D junctions: discontinuously changed doping in graphene supported by a homogeneous dielectric substrate [16, 17], homogeneously doped graphene sheet supported by a wafer with discontinuously changed dielectric permittivity [18], scattering regions, such as a gap in graphene [19, 20], Gaussian-profile spatial distortion of graphene doping [19], and 1D corrugations of graphene sheet [14].

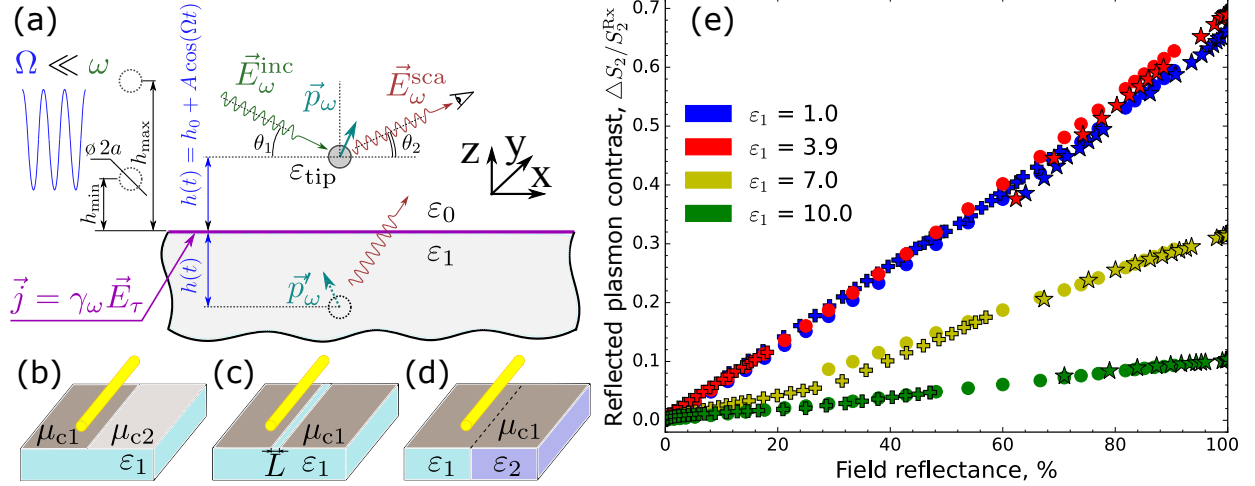


Figure 1: Schematics of s-SNOM of (a) flat dielectric covered by a homogeneous conducting 2D material (see text for details), and three plasmon junction geometries considered in the paper: (b) discontinuous doping, (c) gap in graphene, and (d) discontinuous wafer, sensed by a cylinder s-SNOM tip (sketched in yellow). Panel (e) shows filtered relations between plasmon reflection coefficient and simulated measurements of the S_2 signal contrast (details are explained in the text) for the three different types of junctions and different dielectric permittivities ϵ_1 supporting graphene on the left side of the junctions and ϵ_2 on the right side in a case (d). The junction types (b), (c), and (d) are marked with rounds, stars, and fat pluses, correspondingly.

The electrical conductivity in 2D materials and the dielectric environment above and below define the plasmon wavelength and the electric field distribution—the difference in those physical parameters at two sides of the junction results in a finite reflection coefficient. Therefore, a reverse problem can be solved for the physical properties at one side of the junction using those at another side and reflection coefficient. Measuring the s-SNOM signal over a junction has certain advantages compared to getting the signal from unknown material and a known one used as a reference. The s-SNOM scan of the junction contains an immense amount of information, which is not apparent from simple fitting procedures. Therefore, a more significant amount of parameters can be retrieved by fitting them to a proper model function.

2 Formulation of the Problem

In this work, we develop a model for numerical simulation of the s-SNOM signal of 2D conducting materials taking into account the signal's modulation from the oscillating cylindrical tip, as shown in Fig. 1a. The conductivity γ_ω [21, 22] characterizes a 2D material. In the case of graphene, we assume the Drude model [23] for the conductivity. Our simulations employ a model of s-SNOM of the bare plain surface of a homogeneous dielectric following Refs. [4] and [5]. That model was extended to enable simulations of the s-SNOM of the layered planar structure of homogeneous materials covered by graphene (or other 2D conducting material) [10, 11, 12]. As in the latter references and unlike the original one Ref. [4], we consider the cylindrical tip parallel to the sample surface and thin compared to the characteristic size of the E -field inhomogeneity.

The solution in the Fourier domain makes the problem highly parallelizable. We have achieved an excellent run-time simulation of the s-SNOM scans for three different types, as shown in Fig. 1b-d. We will refer to them as discontinuous conductivity, a gap in graphene, and a discontinuous wafer, correspondingly. We simulated numerous scans for different parameters and verified a technique used by experimentalists for retrieving plasmon reflection coefficients [1]. The main goal of the present research is to determine under which conditions simple assumptions about the s-SNOM S_2 signal across a junction can retrieve a reflection coefficient of the plasmon. The latter can be calculated independently for those junctions [24] and compared with the S_2 signal contrast for different types of junctions and dielectric constants ϵ_1 of the wafer supporting substrates, as shown in Fig. 1e. While the results in Fig. 1e are more or less in agreement with the common-sense assumption [1], namely, the contrast of the S_2 signal is proportional to the reflection coefficient; there are situations when those dependencies can be much more complex. Those cases are not shown in Fig. 1e, but are discussed below. The non-unique relationships between the s-SNOM signal contrast and reflection coefficient are explained by certain arbitrariness in how the s-SNOM scan of a junction can be processed.

3 Basics of the s-SNOM simulations

In the s-SNOM setup, as shown in Fig. 1a, an incident electromagnetic wave with the amplitude $\vec{E}_\omega^{\text{inc}}$ scatters off the tip, which is closely located to the sensed surface. The scattered radiation with the amplitude $\vec{E}_\omega^{\text{sca}}$ (at the point where it is measured) is generated by the varying tip's dipole moment and its reflection in the sensed sample. In the previous models, the scattered far-field was calculated, and the tip's mechanical oscillations were taken into account directly [4, 5, 3], where the angle between the sample's plane and the incident TM polarized wave $\theta_1 \approx 0$ (see Fig. 1a), such that the dipole moment is directed along the z -axis. In the case of a homogeneous surface, this assumption is mathematically self-consistent, and the influence of the mirrored dipole \vec{p}_ω is reduced by a scaling factor of the scattered amplitude $\vec{E}_\omega^{\text{sca}}$. Here, we extend those approaches to the non-homogeneous surface cases with plasmonic junctions (see Figs. 1b-d). If the tip has polarizability in x -direction, the assumption that $\vec{p}_\omega \parallel z$ -axis is no longer valid even if $\theta_1 \approx 0^\circ$. Therefore, our model, along with arbitrary θ_1 and θ_2 , takes into account the tip's polarizability tensor and, correspondingly, an electric field applied to the tip in x -direction. All the plots presented here are calculated for $\theta_1 = 0^\circ$ and $\theta_2 = 0^\circ$. The analysis of the angle dependence is beyond the scope of this work.

The components of the incident field amplitudes $\vec{E}_\omega^{\text{inc}}$ are given by:

$$\vec{E}_\omega^{\text{inc}} = \begin{bmatrix} E_{\omega,x}^{\text{inc}} \\ E_{\omega,z}^{\text{inc}} \end{bmatrix} = E_0 \begin{bmatrix} -\sin \theta_1 \\ \cos \theta_1 \end{bmatrix}, \quad (1)$$

where E_0 is the incident wave's amplitude. For boosting the sensitivity and getting rid of the background signal, which mainly characterizes the tip's size and shape, the tip is forced to oscillate with a mechanical frequency Ω of the cantilever. Therefore, the s-SNOM setup measures the time dependence of $\vec{E}_\omega^{\text{sca}} [h(t)]$, where $h(t)$ is the instant height of the tip's center above the surface. The time-dependent signal is demodulated by a lock-in amplifier producing the resulting signal's series of harmonics:

$$S_n = \frac{2}{T} \int_0^T (\vec{E}_\omega^{\text{sca}}, \vec{\tau}) \cos n\Omega t \, dt, \quad (2)$$

$$T = \frac{2\pi}{\Omega}, \quad \vec{\tau} = \begin{bmatrix} -\sin \theta_2 \\ \cos \theta_2 \end{bmatrix},$$

where the round braces mean the scalar product, and $\vec{\tau}$ is a vector, which direction is determined by the angle θ_2 (see Fig. 1a). As experimentalists ordinarily use the second-order of the demodulated electric field, we show all our results for $n = 2$.

The scalar product $(\vec{E}_\omega^{\text{sca}}, \vec{\tau})$ in Eq. (2) in the Fourier domain is proportional to the amplitude p_ω of the dipole oscillations induced by the incident reference wave and the interaction with the sensed object. Therefore, the relationship between \vec{p}_ω and the input amplitude $\vec{E}_\omega^{\text{inc}}$ of the incident wave determines the S_n signal. Under the assumption of a thin tip, this relationship can be derived if the tip's polarizability tensor $\hat{\alpha}$ and the spatial distribution of E -field $\vec{E}_\omega^{\text{ind}}$ induced by the oscillating dipole moment of the tip \vec{p}_ω are both known. The relationship between $\vec{E}_\omega^{\text{ind}}$ at the center of the tip's dipole and the dipole moment \vec{p}_ω are given by:

$$\vec{E}_\omega^{\text{ind}} = \frac{\hat{\beta}(h) \vec{p}_\omega}{2\varepsilon_0 h^2}, \quad (3)$$

where a tensor $\hat{\beta}$ depends on the properties of the sensed surface and the height of the tip above it. In Ref. [4], where s-SNOM of a bare homogeneous wafer was considered, a similar expression for a point-dipole moment and the induced electric field was derived for the case when \vec{p}_ω is normal to the sensing plane. In that case, $\hat{\beta}$ -tensor is reduced to a scalar value

$$\beta = \frac{\varepsilon_1 - \varepsilon_0}{\varepsilon_1 + \varepsilon_0}, \quad (4)$$

where ε_0 and ε_1 are dielectric permittivities above and below the conducting surface, correspondingly. It corresponds to β_{zz} component of the tensor in the case of sensing a homogeneous bare semi-infinite wafer. Repeating the same derivation for x -components of \vec{p}_ω and $\vec{E}_\omega^{\text{ind}}$, one can show that $\hat{\beta} = \beta \hat{I}$, where \hat{I} is the unity tensor. In our calculations, if not stated otherwise, we will consider 2×2 tensor's dimensions due to the homogeneity in the Y -direction. Eq. (3) is solved together with the following relationship:

$$\vec{p}_\omega = \hat{\alpha} (\vec{E}_\omega^{\text{inc}} + \vec{E}_\omega^{\text{ind}}), \quad (5)$$

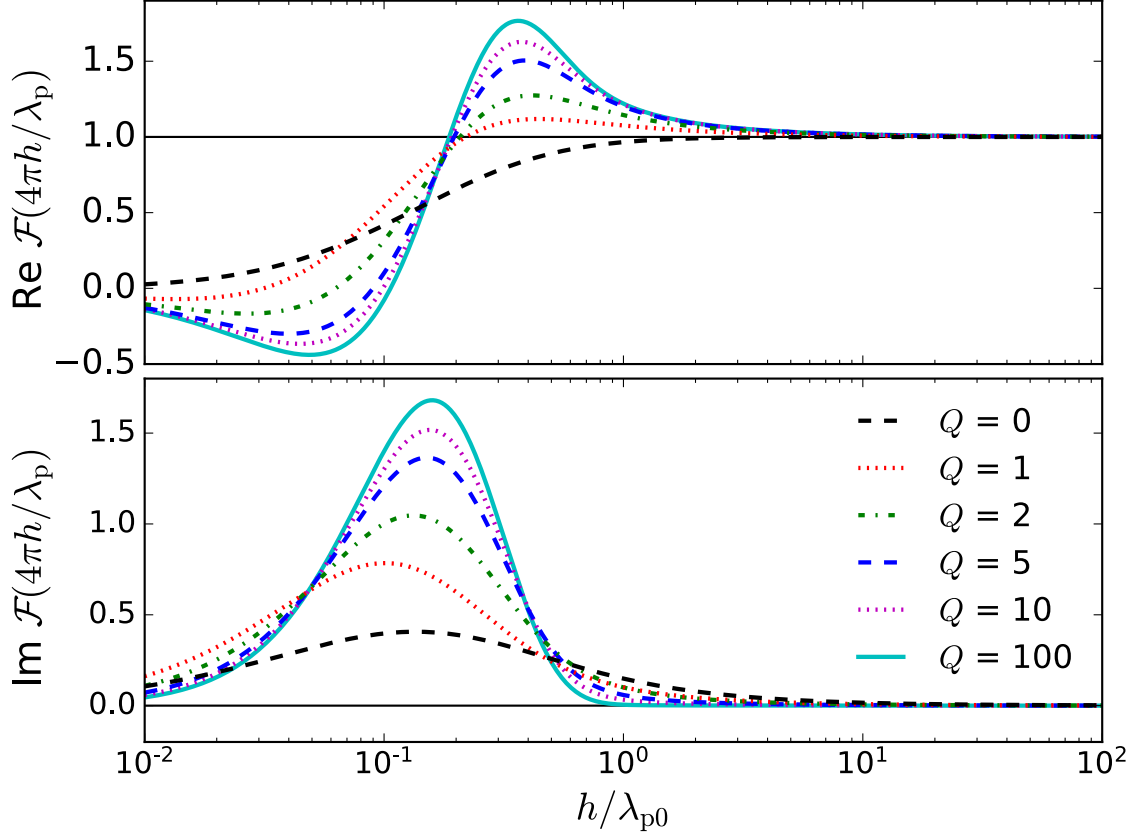


Figure 2: \mathcal{F} complex function versus normalized dipole height h above the sensed surface, calculated for different quality factors of 2D charge density oscillations Q (see text).

where $\hat{\alpha}$ is the tip's polarizability tensor [25]. In the case of a homogeneous, perfectly conducting cylinder, the tensor $\hat{\alpha}$ is reduced to $\alpha\hat{I}$, where $\alpha = \varepsilon_0 a^2/2$, a is tip's radius and \hat{I} is the identity tensor.

Therefore, we obtain:

$$\vec{p}_\omega = \left(\hat{I} - \frac{\hat{\alpha}\hat{\beta}}{2\varepsilon_0 h^2} \right)^{-1} \hat{\alpha} \vec{E}_\omega^{\text{inc}}, \quad (6)$$

where $(\dots)^{-1}$ stands for matrix inversion. One can see that the most challenging part of the calculations is finding components of $\hat{\beta}$ tensor.

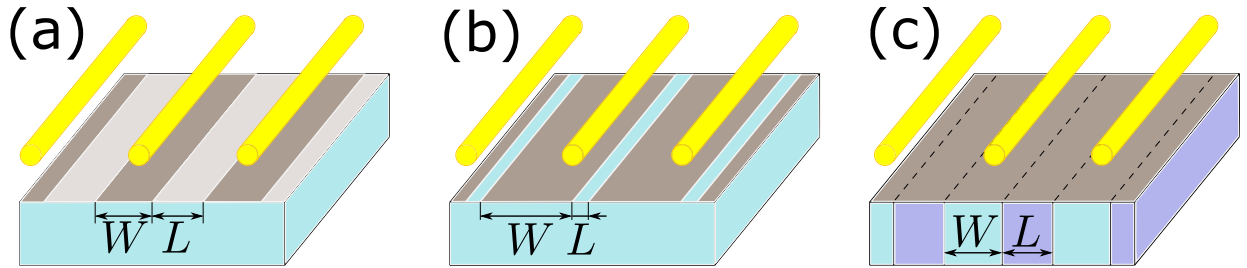


Figure 3: Periodic geometries (a-c) adapted for the numerical analysis we use corresponding to the junctions depicted in Fig. 1b-d.

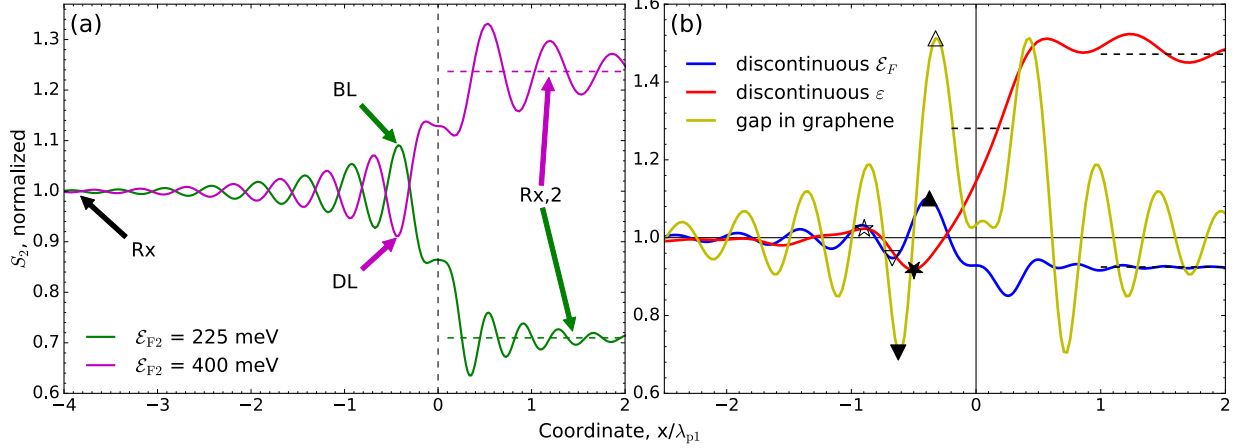


Figure 4: (a) Simulated S_2 scans calculated for two junctions of graphene with discontinuous doping, giving the same reflection coefficient of the plasmon. The relaxed signal value (Rx), brightest (BL), and darkest (DL) lines positions are shown on the left side of the junction. Dielectric permittivity of the wafer supporting the junctions is $\epsilon_1 = 3.9$ and Fermi energy of graphene on the left side is $\mu_{c1} = 300$ meV in both cases. (b) Samples of S_2 scans of all three types of junctions. Parameters of the junctions are the following: (discontinuous doping) $\mu_{c2} = 210$ mV, (discontinuous wafer) $\epsilon_2 = 3.9$, (gap in graphene) $L = 10$ nm. The simulations are done at frequency $\omega = 120$ meV, Fermi energy of the graphene on the left side of a junction $\mu_{c1} = 300$ meV, the dielectric permittivity of a wafer on the left side is $\epsilon_1 = 7.0$, electron scattering rate on both sides of a junction is the same $\nu = 10$ meV, minimum and maximum spans between the tip and the sample are $h_{\min} - a = 5$ nm, $h_{\max} - a = 50$ nm, where $a = 30$ nm is the tip's radius. The whole scans are normalized to the absolute value of the relaxed signal on the junction's left side. The vertical dashed line shows the junction's coordinate. Markers on panel (b) illustrate the classification rules for brightest and darkest lines, which are used to calculate reflected plasmon strength following Eq. (12). Triangle and its variations are used when the plasmon wavelength on the right side of a junction is less than one on the left side. Star and its variations are used in the opposite case when $\lambda_{p2} > \lambda_{p1}$. In the case of a gap in graphene junction, $\lambda_{p2} = 0$ is assumed. Straight oriented markers (\blacktriangle , \triangle , \star and \star) are plot for the case when Eq. (12) is calculated using S_2^{BL} . Their overturned versions (\blacktriangledown , \triangledown , \star , and \star) are plot when S_2^{DL} is used. A solid version of a marker designates a line for which a condition in Eq. (12) is true, and the rest line then is designated with a marker of the same type, but it is opened and oppositely oriented version.

The mirrored dipole moment \vec{p}_ω^{\prime} can be calculated as follows:

$$\vec{p}_\omega^{\prime} = \hat{\beta}' \vec{p}_\omega, \quad \hat{\beta}' = \beta \begin{pmatrix} -1 & 0 \\ 0 & 1 \end{pmatrix}, \quad (7)$$

where β is a scalar factor given by Eq. (4) and expression for $\hat{\beta}'$ applies for a homogeneous bare semi-infinite wafer, which is the same for both small-ball- and thin-rod-like tips.

Before discussing plasmonic junctions, we consider a homogeneous sample to demonstrate $\hat{\beta}'$ calculations. Our analysis shows (see Appendix A) that in the case of a homogeneous conducting surface covering a homogeneous semi-infinite wafer, $\hat{\beta}$ is proportional to \hat{I} as in the case of a bare wafer (see Eq. (4)). However, the coefficient β is different, and it depends on the height h of the dipole above the plane:

$$\beta = \left[1 - \frac{2\epsilon_0}{\epsilon_0 + \epsilon_1} \mathcal{F}(2q_p h) \right], \quad (8)$$

$$\mathcal{F}(\zeta) = \zeta^2 e^{-\zeta} [\text{Ei}(\zeta) + \pi i] - \zeta, \quad (9)$$

$$\text{Ei}(\zeta) = \int_{-\infty}^{\zeta} \frac{e^u}{u} du, \quad q_p = \frac{(\epsilon_0 + \epsilon_1)\omega}{4\pi i \gamma_\omega} \quad (10)$$

where γ_ω is complex conductivity of the 2D surface, and q_p is the complex wavelength of the 2D charge density oscillations (or plasmons) supported by the surface at frequency ω . The complex function $\mathcal{F}(\zeta)$ in Eq. (8) has the following asymptotics: $\mathcal{F}(0) \rightarrow 0$ and $\mathcal{F}(\infty) \rightarrow 1$. In both limits, Eq. (8) reduces to Eq. (4). In the first limit, one

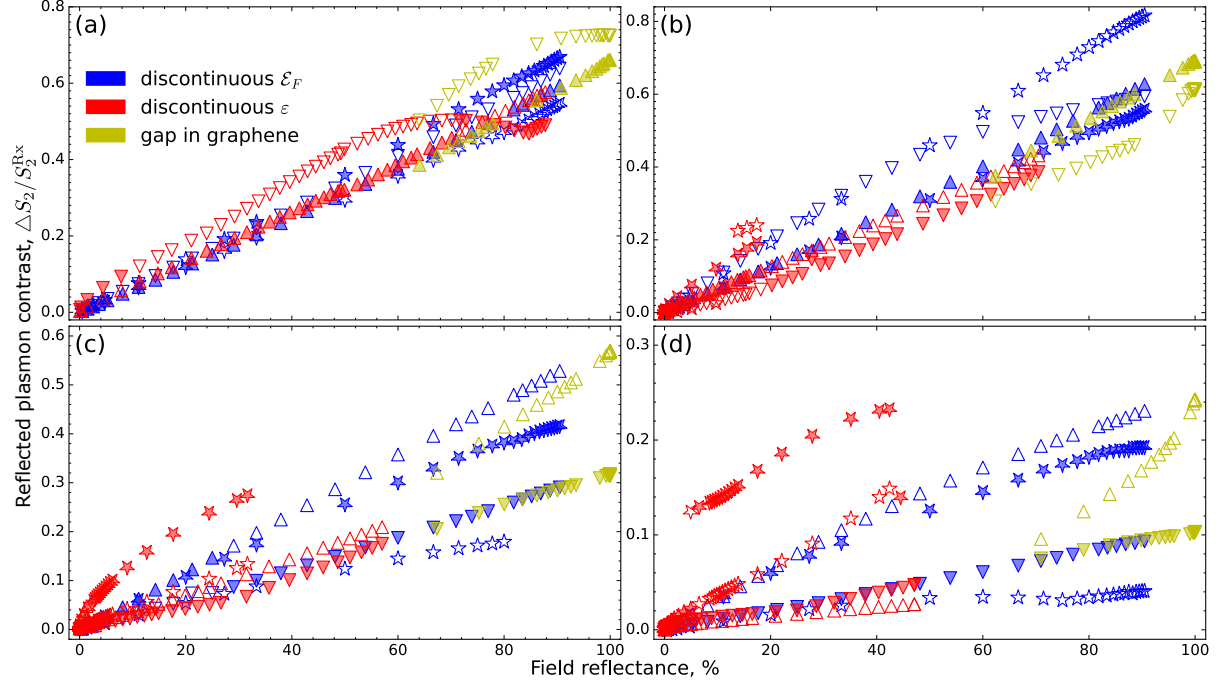


Figure 5: $|S_2|$ signal contrast on the left side of a junction, i.e. S_2 maximum normalized to its relaxed value S_2^{Rxx} , versus modulus of the plasmon reflection coefficient for different dielectric permittivities of the medium below graphene. On the left side of a junction: (a) $\varepsilon_1 = 1.0$, (b) 3.9, (c) 7.0 and (d) 10.0. These simulations are done at fixed $h_{\min} = 35$ nm and $h_{\max} = 80$ nm. All the simulations use graphene's Fermi energy $\mu_c = 300$ meV (or $\mu_{c1} = 300$ meV on the left side of the junction for the case of discontinuous doping junction), electron scattering rate in it $\nu = 10$ meV, and the tip's radius $a = 30$ nm. The markers here have the same meanings as in Fig. 4.

should substitute $\varepsilon_1 \rightarrow \infty$. It means that at $h \ll |q_p^{-1}|$ the dipole interacts with the sample as if it was a perfectly conducting plane and at $h \gg |q_p^{-1}|$ as it was a bare dielectric without conducting surface on the top. To show what happens for intermediate values of ζ , in Fig. 2 we show the dependence of \mathcal{F} on h/λ_{p0} for different “quality factors” Q of the plasmons excitation defined below. Here we assume the Drude-like conductivity γ_ω of the 2D material that in the case of graphene is given by [23]:

$$\gamma_\omega = \frac{e^2 \mathcal{E}_F}{\pi \hbar^2 (i\omega + \nu)}, \quad (11)$$

where \mathcal{E}_F is the Fermi energy and ν is the electron scattering rate. The values of the quality factors $Q = \omega/\nu$ are given in the legend of Fig. 2 for all the cases except for the pure dissipative admittance, in which case $i\omega$ is set to zero in Eq. (11), i.e. $Q = 0$. We define a characteristic length λ_{p0} as: $\lambda_{p0} = 2\pi/\text{Re } q_p$ for $Q > 0$, and $\lambda_{p0} = -2\pi/\text{Im } q_p$, for $Q = 0$.

Eq. (8) corresponds to the case of the reflected near-field signal at the \vec{p}_ω dipole position. If one needs to calculate the field above the tip, at some height H above the sample, the same \mathcal{F} -function can be used with $2h$ replaced by $h + H$ (see the derivation of Eq. (8) in Appendi A). Therefore, since $\mathcal{F}(\infty) \rightarrow 1$ at $H \gg |q_p^{-1}|$, the reflected near-field signal generated by the dipole \vec{p}_ω is the same as if there were no graphene and only a bare wafer were present. Therefore, in the case of a wafer covered by 2D material, $\hat{\beta}^l$ -tensor is the same as for the bare wafer, and it is given by Eq. (7). We can extend this conclusion to the case of 2D material on top of a wafer with spatially non-homogeneous admittance. We have verified this for the case of discontinuous doping junction (see Fig. 1b) by matching calculated reflected near-field at $H \gg |q_p^{-1}|$, h and \vec{E} -field generated by the mirrored dipole \vec{p}_ω given by Eq. (7). In the case of discontinuous wafer junction geometry (see Fig. 1d), $\hat{\beta}^l$ -tensor becomes dependent on the x -coordinate, see Appendix C.2 for more details.

4 Relationship between the plasmon reflection and the S_2 signal contrast

To simulate s-SNOM response in the presence of graphene junctions, we employ a Fourier transform method for periodically repeated junctions, as shown in Figs. 3(a-c). Technically, the Poisson equation solutions in these geometries are exactly the same as in the case of diffraction of the far-field incident on the sample [26, 27, 28]. The only difference is that instead of the far-field, harmonics of the near-field generated by the tip's dipole are "scattered" on the sample (see AppendixC and Ref. [29] for details). To eliminate spurious size effects, we choose the maximal height of the tip's dipole above the sensed surface h_{\max} to be much smaller than the system's period $d = W + L$, and the plasmon's propagation lengths in the regions between the junctions to be much smaller than the lengths W and L .

During the s-SNOM measurements, the tip senses the tip-launched standing wave, resulting from the interference between the tip and the edge-reflected plasmon. The interference pattern disappears at distances larger than the plasmon propagation length. As a result, the S_n signal changes from a constant, which we call a relaxed signal intensity, to an oscillating signal with a growing amplitude as the tip approaches the junction. Examples of the simulated scans are shown in Fig. 4a. This signal behavior is usually used in experiments to determine the coefficient of reflection from the plasmon junctions [1]. It is natural to assume that the envelope of the signal oscillations, normalized to its relaxed value, depends only on the junction's reflection coefficient. The variation of the S_2 signal is considered to be proportional to the reflection coefficient, with the proportionality coefficient being independent of the junction type. This assumption enables one the calibration of the experimental setups using a junction with the known reflection. For instance, it is well known that a graphene edge, or a gap in graphene of the length bigger than about $\lambda_p/4$, almost entirely reflects plasmons [19, 30]. We will show below that such assumptions are not always applicable.

In Fig. 4a, we demonstrate typical S_2 signals for two junctions of graphene with discontinuous Fermi energy supported by a homogeneous substrate. At the junctions, on the left side, the Fermi energies are the same, while on the right side, the Fermi energies are chosen to give the same plasmon reflection coefficients [16, 24]. One can see that in this particular case, the described above assumptions are perfectly justified, i.e. the same reflection gives the same envelope. One of the most straightforward and reasonable estimation of the S_2 signal variation or contrast would be based on fitting the results to an expression like $\pm ae^{b(x-x_0)}$, where x_0 is the junction position. After finding the best-fit parameters a and b , we could agree to define the envelope's half-width as the fitted expression value at some fixed position $x_1 < x_0$ (e.g., at half of the plasmon wavelength to the junction). Our results show that the stated fitting procedure does not work well for processing a broad collection of scans we have simulated. A much more reliable and accurate approach is to define the S_2 contrast as the absolute difference between the brightest (or the darkest) line and the relaxed signal. The choice depends on the relationship between the relaxed signals on the left and the right sides of the junction:

$$\Delta S_2 = \begin{cases} S_2^{\text{BL}} - S_2^{\text{Rx}}, & S_2^{\text{Rx}} > S_2^{\text{Rx},2} \\ S_2^{\text{Rx}} - S_2^{\text{DL}}, & S_2^{\text{Rx}} < S_2^{\text{Rx},2} \end{cases}, \quad (12)$$

where $S_2^{\text{Rx}}, S_2^{\text{Rx},2}$ are the S_2 signals on both sides of the junction measured at the distances where the oscillations are relaxed, and $S_2^{\text{BL}}, S_2^{\text{DL}}$ are the brightest and the darkest lines of the signal scan on the left side of the junction (see Fig. 4a). For the case of a gap in graphene junction, $S_2^{\text{Rx},2}$ is taken as the absolute value of the S_2 signal from the bare wafer, i.e. in the absence of the junction. One should note that Eq. 12 is not the result of some self-consistent mathematical calculation. Instead we choose Eq. 12 definitions because of the similar constructions of S_2^{BL} and S_2^{Rx} have already been used in the experiments. We define S_2 contrast depending on the relation between the relaxed signals at both sides of a junction. To show the conventionality of Eq. 12, we developed a classification of the brightest and darkest lines on the left side of a junction as illustrated in Fig. 4b (see details in the caption).

In Figs. 5(a-d), we plot ΔS_2 normalized to S_2^{Rx} versus the absolute values of the reflection from a junction for different types of junctions and various dielectric permittivities of the wafers supporting the junctions' left sides. Note that plasmon reflections can be calculated independently without involving an s-SNOM tip [16, 18, 24].

It can be concluded from Figs. 5(a-d), that the assumption about the proportionality of the S_2 signal contrast with the reflection coefficient works reasonably well for $\varepsilon_1 = 1$ and $\varepsilon_1 = 3.9$. However, for the larger values of ε_1 , multiple families of curves appear using all alternatives Eq. 12. Moreover, even a single branch does not follow a straight line (see the filled markers). The deviations in Figs 5c,d are most prominent when the plasmon wavelength on the left side of a junction is smaller than on the right side (see star-markers). We relate this to the electric field generated by the long-plasmon-wavelength edge forming the junction. The short-plasmon-wavelength edge does not affect its counterpart because the edge's field penetration length into another side is about half of the plasmon wavelength on the edge's side [24]. Therefore, we find that the assumption about the proportionality between the signal contrast and the plasmon reflection breaks down for the case of a high-k dielectric substrate on the left side of the junction.

5 Conclusion

We applied a model for simulating the s-SNOM signal of 2D conducting for three types of 1D junctions. The model considers the tip oscillation, modulation, and demodulation of the near-field signal. This approach covers a broad range of experimentally relevant parameters. Our numerical approach is time efficient and allows us to explore a wide range of parameters to optimize plasmonic circuits. We provide an analytical model of s-SNOM of a conducting 2D material supported by a dielectric wafer that can be used for choosing a proper regime of the tip's oscillation.

We have analyzed many simulated scans from different types of junctions and found that shapes of s-SNOM signal depend on multiple parameters, such that no simple fitting expression can cover all cases. We have found that the assumption about the proportionality of the S_2 signal contrast and the reflection coefficient works well if a plasmonic junction is deposited on a low-k SiO_2 wafer, but it fails in the cases of high-k substrates. In addition, the assumption breaks down in most cases when the plasmon wavelength at the side of the junction, where the contrast is measured, is smaller than at the other side.

Our findings demonstrate that within the particular parameter space, the s-SNOM response can be used to extract material's properties at the side of the junction, which is non-accessible for the s-SNOM tip. Our computationally efficient approach can generate a large amount of the training data sets for machine learning approaches for processing s-SNOM scans.

Acknowledgments

We acknowledge support from the Vice President for Research and Economic Development (VPRED), SUNY Research Seed Grant Program, and the Center for Computational Research at the University at Buffalo [31].

A The case of homogeneous surface covered conducting 2D material

In this section we present an analytical solution for the tensor's $\hat{\beta}$ components for the homogeneous infinitely thick dielectric wafer. This result is important for understanding the limitations of s-SNOM of 2D conducting materials and analyzing the s-SNOM scans of plasmonic junctions.

The Coulomb field produced by the linear dipole of the tip on the sensing surface are given by:

$$E_x(x) = \frac{-4phx}{(x^2 + h^2)^2}, \quad E_z(x) = \frac{2p(h^2 - x^2)}{(x^2 + h^2)^2}, \quad (13)$$

where h is the height of the dipole above the surface. The Fourier transforms are: $e_{xq} = -2\pi i \cdot pqe^{-|q|h}$, $e_{zq} = 2\pi \cdot p|q|e^{-|q|h}$.

The solution of the Poisson equation can be found as:

$$\varphi^{(r)} = \int_{-\infty}^{\infty} \varphi_q^{(r,0)} e^{i\omega t - iqx - |q|z} \frac{dq}{2\pi}, \quad \varphi^{(t)} = \int_{-\infty}^{\infty} \varphi_q^{(t,0)} e^{i\omega t - iqx + |q|z} \frac{dq}{2\pi}, \quad (14)$$

where $\varphi^{(r)}$ is the potential distribution above the surface (excluding the tip's dipole compound), and $\varphi^{(t)}$ is below it. The boundary conditions at the surface lead to the following relations:

$$\begin{aligned} -p \cdot 2\pi i q e^{-|q|h} + iq\varphi_q^{(r,0)} &= iq\varphi_q^{(t,0)} \\ \varepsilon_0 [p \cdot 2\pi |q| e^{-|q|h} + |q|\varphi_q^{(r,0)}] + \varepsilon_1 |q|\varphi_q^{(t,0)} &= 4\pi\sigma_{\omega,q} \end{aligned} \quad (15)$$

where $\sigma_{\omega,q}$ are the Fourier components of the charge density $\sigma(x,t)$ induced on the surface: $\sigma(x,t) = \int_{-\infty}^{\infty} \sigma_{\omega,q} e^{i\omega t - iqx} \frac{dq}{2\pi}$.

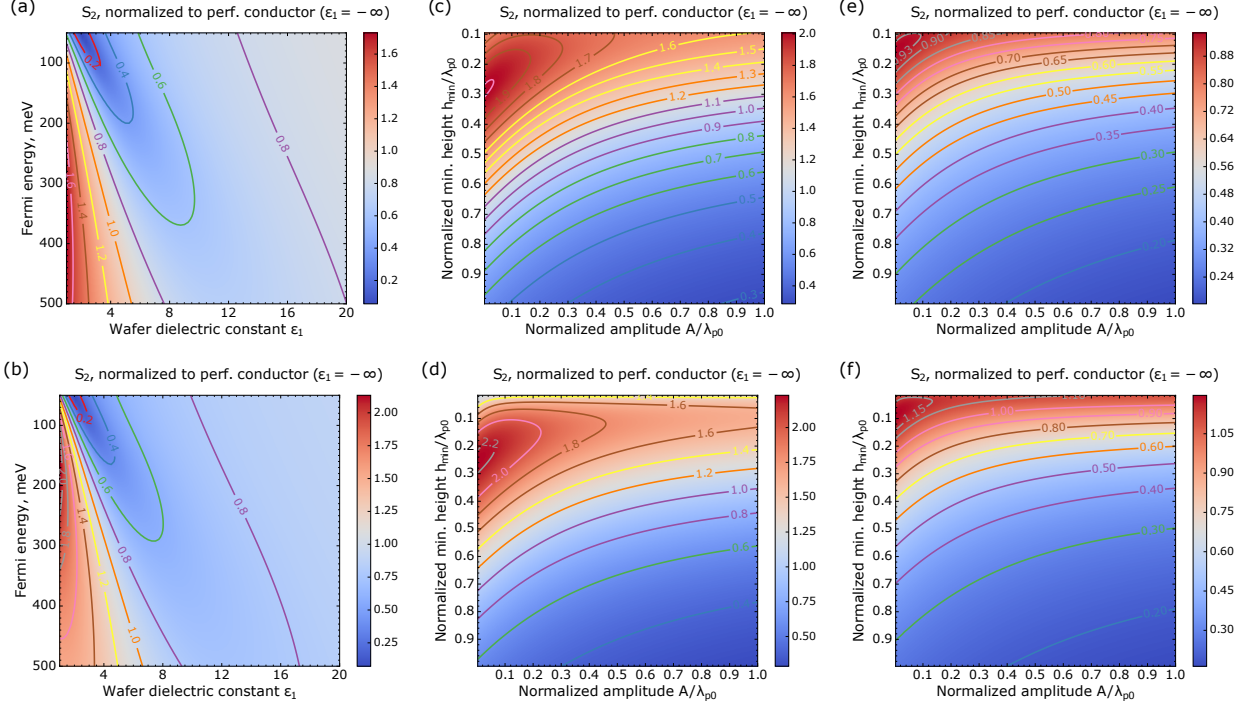


Figure 6: (a) The simulated absolute value of the S_2 signal at frequency $\omega = 120$ meV from graphene with $\nu = 10$ meV, calculated at fixed $h_{\min} = 35$ nm and $h_{\max} = 80$ nm, and plotted versus graphene Fermi energy and wafer's dielectric permittivity. (c) Simulated absolute value of the S_2 signal at ω and ν as in (b), but for fixed Fermi energy of graphene $\mathcal{E}_F = 300$ meV and dielectric permittivity $\varepsilon_1 = 1.0$ below it, plotted versus tip's dipole average height $h_0 = 0.5(h_{\max} + h_{\min})$ and amplitude of mechanical oscillations $A = 0.5(h_{\max} - h_{\min})$ normalized to $\lambda_{p0} = 374$ nm. (e) The same as in (c) but for $\nu = 120$ meV. Tip's radius in panels (a), (c), and (e) is $a = 30$ nm. (b), (d), and (f) The same as in panels (a), (c) and (e), correspondingly, but for tip radius $a = 5$ nm. $|S_2|$ signals at every point of the maps at panels (a-f) are normalized to the values of $|S_2|$ signal of the perfect conductor at the corresponding h_0 , A and a .

We use the continuity equation $\frac{\partial \sigma}{\partial t} + \frac{\partial j}{\partial x} = 0$, where $j(x, t)$ is the linear current in the surface given as $j_{\omega, q} = \gamma_{\omega} E_{x, \omega, q}$, where γ_{ω} is the surface conductivity, $E_{x, \omega, q} = iq\varphi_q^{(t, 0)}$ is the E-field component producing the current in the surface, to obtain $\varphi_q^{(r, 0)}$ and β according to:

$$\beta = \int_{-\infty}^{\infty} \frac{\varepsilon_1 - \varepsilon_0 - 4\pi |q| i\gamma_{\omega}/\omega}{\varepsilon_1 + \varepsilon_0 - 4\pi |q| i\gamma_{\omega}/\omega} |q| e^{-2h|q|} dq \quad (16)$$

After some transformations, Eq. (16) is reduced to

$$\beta = \frac{1}{2\varepsilon_0 h^2} \left[1 - \frac{2\varepsilon_0}{\varepsilon_0 + \varepsilon_1} \mathcal{F}(2q_p h) \right], \quad q_p = \frac{(\varepsilon_0 + \varepsilon_1)\omega}{4\pi i\gamma_{\omega}}, \quad (17)$$

$$\mathcal{F}(\zeta) = \zeta^2 e^{-\zeta} [\text{Ei}(\zeta) + \pi i] - \zeta, \quad \text{Ei}(\zeta) = \int_{-\infty}^{\zeta} \frac{e^u}{u} du,$$

that for $\gamma_{\omega} = 0$ gives the result similar to [5]: $\beta = \frac{\varepsilon_1 - \varepsilon_0}{\varepsilon_0(\varepsilon_1 + \varepsilon_0)} \frac{1}{2h^2}$. Our analysis shows that in the case of the homogeneous conducting surface, $\hat{\beta}$ is also proportional to I as in the case of the bare wafer, but now coefficient β is different and depends on z according to Eq. (17).

Figs. 6 show the results of the absolute value of the S_2 signal from graphene simulation normalized for the one from the perfect conductor for the same tip's radius and CO₂ laser providing the incident beam with wavelength 10.6 μm

that corresponds to 120 meV photon energy. Figs. 6a, b are plotted at standard fixed tip's oscillation regime ($5 \text{ nm} \leq h - a \leq 50 \text{ nm}$) versus graphene Fermi energy \mathcal{E}_F and wafer's dielectric permittivity ε_1 . It is seen that the signal is non-monotonic and the tip's radius does not affect the S_2 signal much. Collating Figs 6c, d, one can conclude that at higher (≥ 10) Q the maximum of the S_2 signal is achieved approximately when the average height of the oscillating dipole h_0 (see description to Fig. 6) corresponds to the maximum of the real part of $\mathcal{F}(\zeta)$, i.e. at $h_0/\lambda_{p0} \approx 0.3$. With decreasing of Q , this ratio decreases (see the panels (e) and (f)) down to zero (the case of $Q = 0$ is not shown for not overloading the figure). Note that despite p_ω dependence not only on h/λ_{p0} , ε_0 and ε_1 (see Eq. (17) and Eqs. (3), (6)), but, at least, on a/h , the scaling of $|S_2|$ versus h_0/λ_{p0} and A/λ_{p0} shown in Figs. 6c-f at the region where both arguments ≥ 0.4 looks universal. This happens because of the normalization to the $|S_2|$ from the perfect conductor simulated at the same tip's radius a , optical frequency ω , and oscillation regime (h_{\min} and h_{\max}).

B s-SNOM of plasmonic junctions

Simulation of the s-SNOM of a plasmonic junction can be done using the same Eqs. (2) and (7) in the main text in the case of sensing a homogeneous surface. The only difference now that the junction breaks homogeneity along the scanning direction and $\hat{\beta}$ (see the definition at Eq. (3) in the main text) now depends on x -coordinate. Also, exact simulation of the signal, even in the framework of our simplified model of dipole line tip and reference wave considered to be parallel to the normal of the sensed surface, must take into account x -component of the dipole moment \vec{p}_ω induced in the tip. Thus, in the general case, in these kinds of simulations, the tensor value $\hat{\beta}$ cannot be reduced to just its single element $\beta = \beta_{zz}$ as it was done in former s-SNOM models. However, in most, but not all cases, which depend on the height of penetration of the evanescent E -field above the surface and the regime of tip's oscillation, one can neglect all but zz -components of $\hat{\beta}$ -tensor and use only β_{zz} component instead of full Eq. (7). Later it will be shown when all the components of $\hat{\beta}$ must be taken into account.

Our work presents the numerical model of s-SNOM of three different graphene plasmonic junctions: graphene doping discontinuity, a gap in graphene, and discontinuity of dielectric permittivity of a wafer supporting homogeneously doped graphene (see Figs. 1b-d in the main text). As it was mentioned in the main text, for the most part, s-SNOM signal simulation is reduced to the solution of the forced problem, in terms of ordinary differential equations theory, giving the relation between the dipole moment oscillations with a fixed amplitude \vec{p}_ω and the E -field in the system generated by it. The forced problem is solved in the periodic domain using Fourier expansion of the unknown function as it's done in the plain wave scattering on graphene grating [27]. The only difference between s-SNOM simulation and plain wave scattering is in the boundary conditions for E -vector and normal D -vector components. Thus, if the E -field vector, generated by the single tip located at $x = 0$ with the dipole moment per unit length \vec{p}_ω , in the vicinity of the sensed surface is $\vec{E}_{\text{st}}(x, \vec{p}_\omega)$, then the total electric field is:

$$\vec{E}_0(x, \vec{p}_\omega) = \sum_{m=-M}^M \vec{E}_{\text{st}}(x - md, \vec{p}_\omega) e^{-im\Phi}, \quad (18)$$

where $M \rightarrow \infty$ and Φ is the phase difference of the dipole moment oscillations between adjacent tips. Once the unit cell length d is big enough as stated above, the result of the S_n simulation does not depend on Φ and it is only needed to be set non-zero to avoid singularity. For calculating the electric field compound generated by the tip's dipole above the surface, one can use the formula analogous to the one for a point dipole, but for the case of the dipole line. For the line of dipoles \vec{p}_ω along the y direction and the position \vec{h} the electric field at \vec{r} is given by:

$$\vec{E}_{\text{st}}(\vec{r}, \vec{p}_\omega) = \frac{4(\vec{p}_\omega, \vec{\rho})}{|\vec{r}|^4} \vec{\rho} - \frac{2\vec{p}_\omega}{|\vec{\rho}|^2}, \quad (19)$$

where $\vec{\rho} = \vec{r} - \vec{h}$ and (\vec{x}, \vec{y}) is the scalar product of the vectors. As we transformed the original geometries to the periodic ones, all the field distributions can be represented in terms of the corresponding Fourier series. Thus, all the equations describing the system are reduced to a set of the linear algebraic equations. The tangential component of the E -vector and the normal component of D -vector spatial distributions at the sensed surface can be represented as:

$$E_{0x} = \frac{1}{2} \sum_{j=-N}^N \varepsilon_{0,j} e^{-iq_j x}, \quad D_{0z} = \frac{1}{2} \sum_{j=-N}^N \Delta_{0,j} e^{-iq_j x}, \quad (20)$$

where $q_j = K + B_0 j$, $K = \Phi/d$ is the quasi-momentum, $B_0 = 2\pi/d$ is the reciprocal unit cell period, and $\varepsilon_{0,j}$, $\Delta_{0,j}$ are complex amplitudes of the Fourier harmonics calculated as:

$$\varepsilon_{0,j}(\vec{p}_\omega) = \frac{2}{d} \int_{-d/2}^{d/2} E_{0x}(x, \vec{p}_\omega) e^{iq_j x} dx, \quad (21)$$

$$\Delta_{0,j}(\vec{p}_\omega) = \frac{2}{d} \int_{-d/2}^{d/2} \varepsilon_0 E_{0z}(x, \vec{p}_\omega) e^{iq_j x} dx.$$

Due to the linearity of the electromagnetic field equations with the dipole moment, its x - and z -components can be considered separately. We solve the self-consistent field excitation problem twice: for $\vec{p}_\omega = p_x \vec{i}$ and $\vec{p}_\omega = p_z \vec{k}$, where \vec{i} and \vec{k} are the unit vectors collinear to the OX and OZ directions, correspondingly. Thus, for the induced electric field back-acting on the tip (see the main text accompanying Eq. (3)) at $\vec{p}_\omega = p_x \vec{i}$ we obtain $\vec{E}_{\text{ind}}^{(p_x)} = p_x [e_{xx}, e_{zx}]$ and at $\vec{p}_\omega = p_z \vec{k}$ it is $\vec{E}_{\text{ind}}^{(p_z)} = p_z [e_{xz}, e_{zz}]$ where $e_{\alpha\beta}$ are components of vectors in XZ -plane to be defined. Once the $e_{\alpha\beta}$ components are known, due to the linearity and superposition principle, one can assemble from them the $\hat{\beta}$ tensor:

$$\hat{\beta} = \begin{pmatrix} e_{xx} & e_{xz} \\ e_{zx} & e_{zz} \end{pmatrix}. \quad (22)$$

Recently plasmon scattering problem for the three types of junctions was solved for the reflection coefficients [24], which are used for the x -axes in Fig. 3d-f (in the main text). The components of $\hat{\beta}$ tensor in Eq. (22) are obtained using the same equations as in Ref. [24] but in the presence of an external field which is unambiguously defined by the Fourier components $\varepsilon_{0,j}$ and $\Delta_{0,j}$. In other words, the forced excitation problem is being solved instead of the eigenmodes calculation. The technical details of getting the solution for the electromagnetic field (and plasmons in particular) are presented in the next section.

C Solution of the forced problem of the electromagnetic field excitation

The representation of electric field above the sensed surface is common for all three periodic geometries:

$$\vec{E}^{(0)}(x, z) = \vec{E}^{(0,\text{ext})}(x, z) + \vec{E}^{(0,\text{refl})}(x, z), \quad (23)$$

$$\vec{E}^{(0,\text{ext})}(x, z) = \sum_{n=-\infty}^{\infty} e^{-in\Phi} \vec{E}_{\text{st}}(\vec{r} - n\vec{d}, \vec{p}_\omega) \quad (24)$$

$$\vec{E}^{(0,\text{refl})}(x, z) = \sum_{j=-\infty}^{\infty} a_j \begin{bmatrix} i\kappa_{0,j} \\ 0 \\ q_j \end{bmatrix} e^{-iq_j x - \kappa_{0,j} z}, \quad (25)$$

where $E^{(0,\text{ext})}$ is the electric field's component produced by the array of tips (here \vec{E}_{st} is the field from a single tip given by Eq. (19), Φ is the phase shift between adjacent unit cells, and \vec{d} is translation vector along X -axis of length $d = W + L$), and $\vec{E}^{(0,\text{refl})}(x, z)$ is the total reflected near field that includes both the component caused by polarization charges in the wafer supporting graphene, and the one caused by the charges induced in graphene, which also can be divided into quasistatic screening charges and oscillating charge density of a plasmon. In the recent equation, a_j are the amplitudes of the reflected field Fourier components, $q_j = K + B_0 j$ and $\kappa_{m,j} = \sqrt{q_j^2 - \varepsilon_m \omega^2 / c^2}$, $\arg \kappa_{m,j} \in (-\pi/2, \dots, \pi/2]$, where $K = \Phi/d$, $B_0 = 2\pi/d$ and ε_m is the dielectric permittivity of the medium labeled by index m .

In the cases of discontinuous doping and wafer geometries (Figs 3a,c), the solution of the problem is found by matching the boundary conditions for the electric fields above and below the sensed surface, that is arranged at $z = 0$. For this purpose, from $\vec{E}^{(0,\text{ext})}(x, z)$ 2D dependence, we need to know only its slice at $z = 0$, namely the tangential component of E -vector $E_{0x} = E_x^{(0,\text{ext})}|_{z=0}$ and the normal component of D -vector $D_{0z} = \varepsilon_0 E_z^{(0,\text{ext})}|_{z=0}$ spatial distributions. As the problem is solved in the spatial Fourier domain, we expand E_{0x} and D_{0z} in Fourier series, and obtain the

corresponding amplitudes of the Fourier harmonics $\varepsilon_{0,j}$ and $\Delta_{0,j}$ using Eqs (21). In the case of a gap-in-graphene junction, from the very beginning, we solved the problem of excitation of quasistatic plasmons, i.e. found the solution of Poisson equation instead of Maxwell equations, using the Coulomb law directly. For this reason, only E_{0x} component and its Fourier series $\varepsilon_{0,j}$ was required from the whole electric field vector distribution $\vec{E}^{(0,\text{ext})}\Big|_{z=0}$.

The resulting solution for plasmons in graphene is found in terms of Fourier series u_j of the spatial distribution of complex amplitudes $j_\omega(x)$ of the linear current oscillations:

$$j(x, t) = \text{Re} e^{i\omega t} j_\omega(x), \quad j_\omega = \frac{1}{2} \sum_{j=-N}^N u_j e^{-iq_j x}. \quad (26)$$

In the following we show the resulting equation systems to be solved for the cases of all three types of junctions.

C.1 Discontinuous doping

$$\begin{aligned} \sum_{m=-N}^N \left[\delta_{jm} - \frac{4\pi i \gamma_\omega}{\omega} \gamma_{jm} \kappa_{0,m} R_m \right] u_m &= \\ &= \gamma_\omega \sum_{m=-\infty}^{\infty} \gamma_{jm} [i\kappa_{0,m} F_m + \varepsilon_{0,m}], \end{aligned} \quad (27)$$

where

$$F_j = \left[\varepsilon_1 \frac{q_j \Xi_j' \varepsilon_{0,j}}{B_0 \gamma_{1,j}} - \Delta_{0,j} \right] / \left[\left(\varepsilon_0 - \varepsilon_1 \frac{i\kappa_{0,j} \Xi_j'}{B_0 \gamma_{1,j}} \right) q_j \right] \quad (28)$$

for $j \neq 0$, otherwise:

$$F_0 = \varepsilon_1 \frac{\Xi_0' \varepsilon_{0,0}}{B_0 \gamma_{1,0}} / \left[\varepsilon_0 - \varepsilon_1 \frac{i\kappa_{0,0} \Xi_0'}{B_0 \gamma_{1,0}} \right], \quad (29)$$

and the values γ_{jm} , R_m , Ξ_j' and $\gamma_{1,j}$ are described in the Appendix of the Ref. [24]. After u_j harmonics are found, the Fourier harmonics a_j of the total reflected near field $\vec{E}^{(0,\text{refl})}$ can be calculated using the following equation:

$$a_j = \frac{4\pi}{\omega} R_j u_j + F_j. \quad (30)$$

C.2 Discontinuous wafer

Here we use a similar approach to Ref. [26]:

$$\begin{aligned} \sum_{\varkappa} \left(\varepsilon_0 \frac{q_j}{\kappa_{0,j}} \varepsilon_{\varkappa j} - 4\pi q_j \frac{i\gamma_\omega}{\omega} \varepsilon_{\varkappa j} - i\Delta_{\varkappa j} \right) C_{\varkappa} &= \\ &= \varepsilon_0 \frac{q_j}{\kappa_{0,j}} \varepsilon_{0,j} - i\Delta_{0,j}, \quad u_j = \gamma_\omega \sum_{\varkappa} \varepsilon_{\varkappa j} C_{\varkappa}, \end{aligned} \quad (31)$$

$$i\kappa_{0,j} a_j + \varepsilon_{0,j} = \sum_{\varkappa} \varepsilon_{\varkappa j} C_{\varkappa}, \quad (32)$$

where $\varkappa = \{\varkappa_l\}$ is the set of roots of the spectral equation described in the Ref. [24], and the summations over \varkappa mean the summation over the root's index l which is omitted in the expressions after Σ for better readability; values $\varepsilon_{\varkappa j}$, $\Delta_{\varkappa j}$ and C_{\varkappa} are also described in the Appendix of the Ref. [24]. After C_{\varkappa} coefficients are found, the Fourier harmonics a_j of the total reflected near field $\vec{E}^{(0,\text{refl})}$ can be calculated using Eq. (32). To calculate $\hat{\beta}^l$ -tensor from Eq. (8) in the main text, we solve Eqs. (31) for horizontally and vertically oriented exciting dipole moment $\vec{p}_\omega = 1 \cdot \vec{i}$ and $\vec{p}_\omega = 1 \cdot \vec{k}$, then knowing a_j we calculate x - and z -components of electric field $E_{x,j}^{(p_x)}$, $E_{z,j}^{(p_x)}$ and $E_{x,j}^{(p_z)}$, $E_{z,j}^{(p_z)}$ using Eq. (25) at some

certain height $\sim 2 \div 3z$ above the sample and at $x = 0$. Then, we calculate the base harmonics of \vec{E} -field produced by the same p_ω -dipole located at the same x -coordinate and negative z -coordinate:

$$\begin{aligned} E_{x0,j}^{(p_x)} &= \varepsilon_{0,j} \left(1 \cdot \vec{i}\right) e^{-\kappa_{0,j} z}, \\ E_{z0,j}^{(p_x)} &= -\Delta_{0,j} \left(1 \cdot \vec{i}\right) e^{-\kappa_{0,j} z} / \varepsilon_0, \\ E_{x0,j}^{(p_z)} &= -\varepsilon_{0,j} \left(1 \cdot \vec{k}\right) e^{-\kappa_{0,j} z}, \\ E_{z0,j}^{(p_z)} &= \Delta_{0,j} \left(1 \cdot \vec{k}\right) e^{-\kappa_{0,j} z} / \varepsilon_0, \end{aligned} \quad (33)$$

where $\varepsilon_{0,j}(\vec{p}_\omega)$ and $\Delta_{0,j}(\vec{p}_\omega)$ are given by Eqs. (21). Then the components of β^l -tensor are found from the following equations:

$$\begin{pmatrix} E_{x0,j}^{(p_x)} & E_{x0,j}^{(p_z)} \\ E_{z0,j}^{(p_x)} & E_{z0,j}^{(p_z)} \end{pmatrix} \begin{pmatrix} \beta_{xx}^l & \beta_{zx}^l \\ \beta_{xz}^l & \beta_{zz}^l \end{pmatrix} = \begin{pmatrix} E_x^{(p_x)} & E_x^{(p_z)} \\ E_z^{(p_x)} & E_z^{(p_z)} \end{pmatrix}. \quad (34)$$

As a result, β^l -tensor is found with the high accuracy, and its value remains constant while $z \ll d$.

C.3 Gap in graphene

The same approach for the case of similar and non-periodic geometry was considered before in Ref. [29].

$$\sum_{l=-N}^N \left(\delta_{jl} - \frac{i\gamma_\omega}{\omega} \frac{\pi B_0'}{\varkappa} M_{jl} \right) u_l' = \frac{1}{\varkappa} \gamma_\omega \varepsilon_{0,j}', \quad (35)$$

$$\sum_{l=-N}^N (-1)^l u_l' = 0, \quad \varkappa = \frac{\varepsilon_0 + \varepsilon_1}{2}, \quad B_0' = \frac{2\pi}{W}, \quad (36)$$

where

$$M_{jl} = M_{jl}^{(0)} + \sum_{k=1}^K \left(M_{jl}^{(k,a)} \cos k\Phi - M_{jl}^{(k,s)} \sin k\Phi \right), \quad (37)$$

where $\varepsilon_{0,j}'$ and u_l' are Fourier expansions of $E_{0x}(x)$ and $j_\omega(x)$ on shorter range $(-W/2..W/2)$ than their actual period d :

$$\begin{aligned} \varepsilon_{0,j}' &= \frac{2}{W} \int_{-W/2}^{W/2} E_{0x}(x) e^{iB_0' j x} dx, \\ u_j' &= \frac{2}{W} \int_{-W/2}^{W/2} j_\omega(x) e^{iB_0' j x} dx, \end{aligned} \quad (38)$$

K is the number of neighbors of a graphene ribbon are taken into account and the values $M_{jl}^{(0)}$, $M_{jl}^{(k,a)}$, and $M_{jl}^{(k,s)}$ are described in the Appendix of the Ref. [24]. After u_j' complex harmonics are calculated, they are transformed to the s_j' harmonics using the charge conservation equation $\frac{\partial \sigma}{\partial t} + \frac{\partial j}{\partial x} = 0$, or $s_j' = j B_0' / \omega \cdot u_j'$, and then s_j' are transformed to the harmonics of the Fourier expansion of the periodic function $\sigma_\omega(x)$ in the Bloch representation of the charge density oscillation $\sigma(x, t)$ in the whole sensed surface:

$$\sigma(x, t) = \text{Re} e^{i\omega t} \sigma_\omega(x), \quad \sigma_\omega = \frac{1}{2} \sum_{j=-N}^N s_j e^{-iq_j x},$$

where $q_j = K + B_0 j$ (K and B_0 are defined above).

Once the surface charge density distribution $\sigma(x, t)$ and its Fourier expansion s_j are known, one can solve the Poisson equation and find the corresponding to it electrostatic potential distribution in the regions above and below the surface $z = 0$ in the following form:

$$\varphi^{\text{surf}}(x, z) = \frac{1}{2} \sum_{j=-N}^N \varphi_j e^{-iq_j x \mp |q_j| z}, \quad (39)$$

where the sign “-” corresponds to the region $z \geq 0$, and “+” to $z < 0$. Solution of the Poisson equation gives:

$$\varphi_j = \frac{2\pi s_j}{\varkappa q_j}.$$

Knowing φ^{surf} , one can calculate the corresponding to it electric field $\vec{E}^{\text{surf}} = -\frac{\partial}{\partial \vec{r}} \varphi^{\text{surf}}$, and to obtain the total near electric field reflected from the sensed sample, we need to add the component associated with the polarization charges in the wafer supporting the graphene: $\vec{E}^{\text{(0,refl)}} = \vec{E}^{\text{surf}} + \vec{E}^{\text{bulk}}$, where

$$\vec{E}^{\text{bulk}} = \frac{\varepsilon_1 - \varepsilon_0}{\varepsilon_1 + \varepsilon_0} \sum_{j=-\infty}^{\infty} \begin{bmatrix} -\varepsilon_{0,j} \\ 0 \\ \frac{\Delta_{0,j}}{\varepsilon_0} \end{bmatrix} e^{-iq_j x - |q_j| z},$$

where $\varepsilon_{0,j}$ and $\Delta_{0,j}$ are calculated above using Eq. (21).

References

- [1] L. Jiang, Z. Shi, B. Zeng, S. Wang, J.-H. Kang, T. Joshi, C. Jin, L. Ju, J. Kim, T. Lyu, Y.-R. Shen, M. Crommie, H.-J. Gao, and F. Wang. Soliton-dependent plasmon reflection at bilayer graphene domain walls. *Nature Materials*, 15:840–845, 2016.
- [2] L. Xiong, Forsythe C., M. Jung, A.S. McLeod, S.S. Sunku, Y.M. Shao, G.X. Ni, A.J. Sternbach, S. Liu, J.H. Edgar, E.J. Mele, M.M. Fogler, G. Shvets, C.R. Dean, and Basov. D.N. Photonic crystal for graphene plasmons. *Nature Communications*, 10:4780, 2019.
- [3] J. Zhang, X. Chen, S. Mills, T. Ciavatti, Z. Yao, R. Mescall, H. Hu, V. Semenenko, Z. Fei, H. Li, V. Perebeinos, H. Tao, Q. Dai, X. Du, and M. Liu. Terahertz nanoimaging of graphene. *ACS Photonics*, 5(7):2645–2651, 2018.
- [4] Bernhard Knoll and Fritz Keilmann. Enhanced dielectric contrast in scattering-type scanning near-field optical microscopy. *Optics Communications*, 182(4):321 – 328, 2000.
- [5] R. Hillenbrand, B. Knoll, and F. Keilmann. Pure optical contrast in scattering-type scanning near-field microscopy. *J. of Microscopy*, 202(1):77–83, 2001.
- [6] A. Cvitkovic, N. Ocelic, and R. Hillenbrand. Analytical model for quantitative prediction of material contrasts in scattering-type near-field optical microscopy. *Opt. Ex.*, 15(14):8550, 2007.
- [7] Alexander S. McLeod, P. Kelly, M. D. Goldflam, Z. Gainsforth, A. J. Westphal, Gerardo Dominguez, Mark H. Thiemens, Michael M. Fogler, and D. N. Basov. Model for quantitative tip-enhanced spectroscopy and the extraction of nanoscale-resolved optical constants. *Phys. Rev. B*, 90:085136, Aug 2014.
- [8] B.-Y. Jiang, L. M. Zhang, A. H. Castro Neto, D. N. Basov, and M. M. Fogler. Generalized spectral method for near-field optical microscopy. *Journal of Applied Physics*, 119(5):054305, 2016.
- [9] S. Chui, Mengkun Liu, Xinzhong Chen, Zhifang Lin, and Jian Zi. Scattering of electromagnetic waves from a cone with conformal mapping: Application to scanning near-field optical microscope. *Physical Review B*, 97, 01 2018.
- [10] Javier Aizpurua, Thomas Taubner, F. Javier García de Abajo, Markus Brehm, and Rainer Hillenbrand. Substrate-enhanced infrared near-field spectroscopy. *Opt. Express*, 16(3):1529–1545, Feb 2008.
- [11] Zhe Fei, G. Andreev, Wenzhong Bao, Lingfeng Zhang, Alexander McLeod, Chen Wang, Margaret Stewart, Zeng Zhao, Gerardo Dominguez, Mark Thiemens, Michael Fogler, Michael Tauber, Antonio Castro Neto, Jeanie Lau, Fritz Keilmann, and Dimitri Basov. Infrared nanoscopy of dirac plasmons at the graphene-sio2 interface. *Nano letters*, 11:4701–5, 11 2011.

- [12] Z. Yao, V. Semenenko, J. Zhang, S. Mills, X. Zhao, X. Chen, H. Hu, R. Mescall, T. Ciavatti, S. March, S. R. Bank, T. H. Tao, X. Zhang, V. Perebeinos, Q. Dai, X. Du, and M. Liu. Photo-induced terahertz near-field dynamics of graphene/InAs heterostructures. *Opt. Ex.*, 27(10):13611, 2019.
- [13] J. Chen, M. L. Nesterov, A. Ju. Nikitin, S. Thongrattanasiri, P. Alonso-González, T. M. Slipchenko, F. Speck, M. Ostler, T. Seyller, I. Crassee, F. H. L. Koppens, L. Martin-Moreno, J. G. Abajo, A. B. Kuzmenko, and R. Hillenbrand. Strong plasmon reflection at nanometer-size gaps in monolayer graphene on sic. *ACS Nano*, 13(12):6210–6215, 2013.
- [14] T. M. Slipchenko, M. L. Nesterov, R. Hillenbrand, A. Yu. Nikitin, and L. Martin-Moreno. Graphene plasmon reflection by corrugations. *ACS Photonics*, 4(9):3081–3088, 2017.
- [15] Xinzhong Chen, Richard Ren, and Mengkun Liu. Validity of machine learning in the quantitative analysis of complex scanning near-field optical microscopy signals using simulated data. *Physical review applied*, 15(1):014001, 2021.
- [16] B. Rejaei and A. Khavasi. Scattering of surface plasmons on graphene by a discontinuity in surface conductivity. *J. Opt.*, 17:075002, 2015.
- [17] S. Farajollahi, B. Rejaei, and A. Khavasi. Reflection and transmission of obliquely incident graphene plasmons by discontinuities in surface conductivity: observation of the brewster-like effect. *J. Opt.*, 18:075005, 2016.
- [18] A. J. Chaves, B. Amorim, Yu. V. Bludov, P. A. D. Goncalves, and N. M. R. Peres. Scattering of graphene plasmons at abrupt interfaces: An analytic and numeric study. *Phys. Rev. B*, 97:035434, 2018.
- [19] J. L. Garcia-Pomar, A. Yu. Nikitin, and Martin-Moreno L. Scattering of graphene plasmons by defects in the graphene sheet. *ACS Nano*, 7(6):4988–4994, 2013.
- [20] B.-Y. Jiang, E. J. Mele, and M. Fogler. Theory of plasmon reflection by a 1d junction. *Opt. Ex.*, 26(13):17209, 2018.
- [21] Fengnian Xia, Han Wang, Di Xiao, Madan Dubey, and Ashwin Ramasubramaniam. Two-dimensional material nanophotonics. *Nature Photonics*, 8(12):899–907, Dec 2014.
- [22] Ganesh R. Bhimanapati, Zhong Lin, Vincent Meunier, Yeonwoong Jung, Judy Cha, Saptarshi Das, Di Xiao, Youngwoo Son, Michael S. Strano, Valentino R. Cooper, Liangbo Liang, Steven G. Louie, Emilie Ringe, Wu Zhou, Steve S. Kim, Rajesh R. Naik, Bobby G. Sumpter, Humberto Terrones, Fengnian Xia, Yeliang Wang, Jun Zhu, Deji Akinwande, Nasim Alem, Jon A. Schuller, Raymond E. Schaak, Mauricio Terrones, and Joshua A. Robinson. Recent advances in two-dimensional materials beyond graphene. *ACS Nano*, 9(12):11509–11539, 2015. PMID: 26544756.
- [23] G. W. Hanson. Dyadic green’s functions and guided surface waves for a surface conductivity model of graphene. *J. Appl. Phys.*, 103:064302, 2008.
- [24] Vyacheslav Semenenko, Mengkun Liu, and Vasili Perebeinos. Scattering of quasistatic plasmons from one-dimensional junctions of graphene: Transfer matrices, fresnel relations, and nonlocality. *Phys. Rev. Applied*, 14:024049, Aug 2020.
- [25] Alexandre Bouhelier, Michael R. Beversluis, and Lukas Novotny. Near-field scattering of longitudinal fields. *Applied Physics Letters*, 82(25):4596–4598, 2003.
- [26] P. Sheng, R. S. Stepleman, and P. N. Sanda. Exact eigenfunctions of square-wave gratings: Application to diffraction and surface-plasmon calculation. *Phys. Rev. B*, 26(6):2907, 1982.
- [27] V. Semenenko, S. Schuler, A. Centeno, A. Zurutuza, T. Mueller, and V. Perebeinos. Plasmon-plasmon interactions and radiative damping of graphene plasmons. *ACS Photonics*, 5(9):3459–3465, 2018.
- [28] O. Klimenko, S. Schuler, A. Muratov, V. Semenenko, E. Gorbachev, T. Mueller, and V. Perebeinos. Tunable graphene plasmons in nanoribbon arrays: the role of interactions. *Opt. Mater. Express*, 11(5):1390–1400, May 2021.
- [29] A. V. Arsenin, A. D. Gladun, V. G. Leiman, V. L. Semenenko, and V. I. Ryzhii. Plasma oscillations of the two-dimensional electron gas in the field-effect transistor with a cylindrical gate electrode. *J. Comm. Tech. E.*, 55(11):1285–1294, 2010.
- [30] A. Yu. Nikitin, T. Low, and Martin-Moreno L. Anomalous reflection phase of graphene plasmons and its influence on resonators. *Phys. Rev. B*, 90:041407(R), 2014.
- [31] Center for Computational Research, University at Buffalo. <http://hdl.handle.net/10477/79221>.